Incorporating decoherence into solid-state time-dependent density functional theory

Isabella Floss,[1,*] Christoph Lemell,[1] Kazuhiro Yabana,[2,3] and Joachim Burgdörfer[1]

[1]*Institute for Theoretical Physics, Vienna University of Technology, Wiedner Hauptstr. 8-10, A-1040 Vienna, Austria, European Union*

[2]*Center for Computational Sciences, University of Tsukuba, Tsukuba 305-8577, Japan*

[3]*Graduate School of Pure and Applied Sciences, University of Tsukuba, Tsukuba 305-8571, Japan*

(Received 27 March 2019; revised manuscript received 13 May 2019; published 3 June 2019)

Time-dependent density functional theory (TDDFT) has developed into an efficient and versatile description of realistic extended many-electron systems driven, e.g., by strong laser fields. It accounts for the fully coherent evolution of the N-electron wave packet representing an isolated system. Decoherence as encountered in open systems by coupling to external degrees of freedom of a bath of, e.g., phonons or defects, is, by construction, absent. In this work we present an open-quantum system (OQS) extension of TDDFT accounting for dephasing and decoherence due to electron-phonon or defect scattering. We test the OQS-TDDFT for high-harmonic generation and irreversible changes of dielectric properties in solids driven by strong ir and mid-ir laser pulses. We present applications to diamond as a prototypical wide band-gap dielectric. For weak pulses we demonstrate the equivalence of OQS-TDDFT with the solution of the Bloch equations for the reduced one-particle density matrix while differences appear at high excitation densities. Our study highlights the importance of the accurate representation of the band structure in simulations of the harmonic spectrum. Narrow avoided crossings within the Brillouin zone can give rise to Bloch-type oscillations.

DOI: 10.1103/PhysRevB.99.224301

I. INTRODUCTION

The description of the electronic system of solids is notoriously difficult to achieve due to the large number of interacting particles involved in the extended system and requires drastic simplifications. One of the most successful methods for the determination of the ground state in many-electron systems is density functional theory [1] (DFT) based on the notion that all physical observables of any system can be expressed as functionals of the local density $n(\vec{r})$. The extension of DFT to model the dynamics of time-dependent electronic systems is founded on the Runge-Gross theorem [2] setting the stage for a plethora of investigations of systems interacting with time-dependent external potentials $V_{\rm ext}(t)$. Incorporating periodic boundary conditions in crystalline solids, it became possible to study the electronic dynamics in solids driven by strong and short laser pulses [3]. While many physical observables can be accounted for by TDDFT, in particular in the linear-response regime for weak pulses, major challenges remain.

One current topical case in point is the high-harmonic generation (HHG) spectrum, the highly nonlinear optical response of solids. While experiments display a sequence of well-pronounced odd harmonics in the so-called "plateau regime" at frequencies well above the band gap [4–7], standard effective single-particle Schrödinger equations [8,9], or solutions of the Kohn-Sham equations of TDDFT [10–12] display noisy and largely structureless high-frequency spectra in the nonperturbative regime. Pronounced harmonics are only recognizable for low orders inside or just above the band gap. It was therefore proposed that dephasing and decoherence of the driven electronic wave packet along the excursion inside the solid might be responsible for this discrepancy [5,6,8,13,14] as excited electrons in a solid will suffer elastic and inelastic scattering events with, e.g., phonons, crystal defects, impurities, or at higher excitation densities, undergo electron-electron scattering.

Extension of TDDFT and time-dependent current density functional theory (TDCDFT) to open quantum systems is still a widely open problem. Extensions of the Runge-Gross theorem [2] using a master equation approach [15] or stochastic methods [16–18] have been presented for interacting many-electron systems. To account for the dephasing influence of higher-order terms of the BBGKY hierarchy [19] on the coherence of the one-particle reduced density matrix [1RDM and its diagonal elements, the one-particle density $n(\vec{r},t)$] exchange-correlation functionals with memory kernels have been proposed [20–23]. In the stochastic mean-field approach [24] closely related to the truncated Wigner approximations [25], initial correlations are included in the propagation through stochastic ensembles of density matrices. Alternatively, electron-electron collisions have been explicitly included during the propagation in terms of Boltzmann-type collision kernels within the framework of the stochastic time-dependent Hartree-Fock (STDHF) approximation [26,27]. Applications to realistic three-dimensional (3D) solids and to the regime of nonlinear driving have remained an unsolved problem. Extensions of TDDFT to the electronic systems with coupling to environmental degrees of freedom [28–31] have so far only been presented for atoms, molecules, or small model systems. Yet, an operational protocol for the implementation in real-space real-time TDDFT simulations of extended systems appears to be missing.

In the present work we extend the TDDFT simulations of laser-solid interactions to an open-quantum system (OQS-)

*Corresponding author: isabella.floss@tuwien.ac.at

TDDFT. The electronic system described by TDDFT is allowed to interact with external ("environmental") degrees of freedom representing, e.g., phonons or lattice defects. We focus on dephasing and decoherence in the electronic system induced by an external bath rather than on decohering effects of intrinsic multiparticle correlations on the 1RDM accounted for by memory kernels. System-bath interactions allow for energy exchange, induce stochastically fluctuating phases and, eventually, dephasing of the electronic wave packet. Including these processes consistently while preserving the properties of the time evolution of the nonlinear Kohn-Sham (KS) equations, most importantly the particle number, is key for a successful implementation of OQS-TDDFT. For the present case of laser-solid interactions we exploit Houston orbitals as the pointer states of decoherence [32]. The method outlined in the following is, however, general and is applicable for a wide array of nonequilibrium scenarios. The present approach can be viewed as the extension of stochastic wave-function methods [18] or Lindblad-Redfield approaches [33,34] to the realm of TDDFT. As a first proof of principle we demonstrate the equivalence of the present OQS-TDDFT with the Bloch equation (BE) approach to the time-dependent one-body reduced density matrix (TD-1RDM), when using the same ground-state DFT input for the band structure and dipole coupling matrix elements and the same phenomenological decoherence or dephasing rate $1/\tau_{\rm dec} = 1/T_2$. This correspondence holds remarkably well for weak fields and even for moderately strong fields when the applicability of electronic ground-state properties is, *a priori*, not obvious. We demonstrate this equivalence for high-harmonic spectra. Decoherence is found to be primarily responsible for modifying the nonlinear response at late times and suppressing the induced post-pulse currents. OQS-TDDFT allows one, however, to go beyond the weak-field limit and to simulate the strong-field regime approaching the dielectric break-down regime. One hallmark of decoherent dynamics is the irreversible electronic excitations from the valence band to the conduction band at the conclusion of the pulse modifying the dielectric properties of the medium.

In Sec. II we briefly review the present implementation of the real-time real-space TDDFT. Its generalization to an open quantum system approach, OQS-TDDFT, is introduced in Sec. III. We benchmark the OQS-TDDFT against the TD-1RDM evolution using the standard Bloch equations and demonstrate the importance of accounting for decoherence in the calculation of the linear and nonlinear response of diamond in Sec. IV. Atomic units ($e = \hbar = m_e = 1$) are used throughout this paper unless otherwise stated.

II. TIME-DEPENDENT DENSITY FUNCTIONAL THEORY

In the present real-space real-time formulation [3] of TDDFT describing the nonlinear electron dynamics induced by strong and short laser pulses in crystalline insulators we solve the time-dependent Kohn-Sham (KS) equations,

$$i\partial_t u_{n\vec{k}}(\vec{r},t) = \hat{H}^{\rm KS}_{\vec{k}}(t)\, u_{n\vec{k}}(\vec{r},t), \tag{1}$$

with the KS Hamiltonian,

$$\hat{H}^{\rm KS}_{\vec{k}}(t) = \tfrac{1}{2}(\vec{p}+\vec{k}+\vec{A}(t))^2 + V_{\rm KS}[n(\vec{r},t)], \tag{2}$$

for the periodic orbitals $u_{n\vec{k}}(\vec{r},t)$ entering the Bloch wave functions for periodic potentials,

$$\phi_{n\vec{k}}(\vec{r},t) = e^{i\vec{k}\vec{r}}u_{n\vec{k}}(\vec{r},t). \tag{3}$$

The electron-electron and electron-ion interactions and the exchange-correlation (XC) potential are included in the effective one-electron KS potential $V_{\rm KS}[n(\vec{r},t)]$, a functional of the local electron density $n(\vec{r},t)$. In this work we use the local-density approximation (LDA) to $V_{\rm XC}$ with the parametrization of Perdew and Zunger [35]. The method for implementing the open-quantum system approach presented in this paper is, however, independent of the choice of the exchange-correlation potential. The coupling to the radiation field in terms of the vector potential $\vec{A}(t)$ in dipole approximation $\vec{A}(t) = -\int_{-\infty}^{t} dt'\vec{F}(t')$ with $\vec{F}(t)$ the electric field employs the velocity gauge [Eq. (2)] in order to preserve the periodicity of the Bloch states in the presence of the strong field.

A suitable basis for expanding the periodic orbital $u_{n\vec{k}}(\vec{r},t)$ in the presence of the $\vec{A}(t)$ field are the Houston orbitals [36,37],

$$u^{\rm H}_{n\vec{k}}(\vec{r},t) = \exp\left(-i\int^{t} dt'\varepsilon_{n\vec{k}+\vec{A}(t')}\right)u^{\rm GS}_{n\vec{k}+\vec{A}(t)}(\vec{r}\,), \tag{4}$$

where $u^{\rm GS}_{n\vec{k}+\vec{A}(t)}$ are the ground-state orbitals shifted by $\vec{A}(t)$ in $\vec{k}$ space with an additional global phase factor depending on the eigenenergies $\varepsilon_{n\vec{k}}$. They resemble the Volkov states [38] employed in strong-field atomic and molecular physics and represent the solution of Eq. (1) in the adiabatic limit of slowly varying $\vec{A}(t)$. The expansion of the time-dependent periodic orbitals in Houston orbitals,

$$u_{n\vec{k}}(\vec{r},t) = \sum_{i=1}^{N_{\rm vb}}\alpha_{in\vec{k}}u^{\rm H}_{i\vec{k}}(\vec{r},t) + \sum_{i=1}^{N_{\rm cb}}\beta_{in\vec{k}}u^{\rm H}_{i+N_{\rm vb}\vec{k}}(\vec{r},t), \tag{5}$$

carries the key advantage that the number of bands required to be included in converged calculations can be restricted to those that are nonadiabatically coupled, preferentially near avoided crossings in the band structure. Moreover, Eq. (5) allows for a well-defined separation into $N_{\rm vb}$ valence- and $N_{\rm cb}$ conduction-band contributions. These properties will also play a key role in our implementation of decoherent dynamics.

For the simulation results presented in this paper we choose diamond as prototypical wide band gap dielectric solid. The cuboid $4.77 \times 4.77 \times 6.74$ a.u.^{3} unit cell is discretized on a Cartesian grid with spacing 0.21 a.u. and 0.29 a.u. parallel and orthogonal to the polarization direction of the laser pulse polarized parallel to the $\Gamma - X$ direction. This unit cell contains four C atoms of which the inner shell $1s^2$ electrons are frozen and included in norm-conserving pseudopotentials of the Troullier-Martins form [39]. In reciprocal space we apply a Cartesian grid with spacing 0.02 a.u. and 0.07 a.u. parallel and orthogonal to the polarization direction, respectively. For the time propagation we employ a fourth-order Taylor expansion using a time step of $\Delta t_{\rm TDDFT} = 0.015$ a.u. All discretization parameters were carefully checked for numerical convergence. We will consider the electronic dynamics in diamond driven by few-cycle strong linearly polarized laser pulses $\vec{F}(t)$, either by an infrared pulse with $\lambda = 800$ nm corresponding a cycle period of $T \approx 2.7$ fs or a mid-ir pulse

with $\lambda = 3200$ nm with $T \approx 10.7$ fs. With increasing cycle period the influence of dephasing is expected to increase even for few-cycle pulses.

The physical observables considered in the following can be extracted from the induced current density averaged over the unit cell volume V_c,

$$\vec{J}(t) = -\frac{i}{V_c}\int_{V_c} d^3r \sum_{n\vec{k}} \phi^*_{n\vec{k}}(\vec{r},t)[\hat{H}^{\mathrm{KS}}(t),\hat{\vec{r}}]\phi_{n\vec{k}}(\vec{r},t), \quad (6)$$

which is directly accessible from the TDDFT orbitals. In particular, the HHG spectrum can be calculated using Larmor's formula [40],

$$S_{\hat{n}}(\omega) \propto \left|\mathfrak{Ft}\left\{\frac{d}{dt}\vec{J}(t)\cdot\hat{n}\right\}\right|^2 = \omega^2|\vec{J}(\omega)\cdot\hat{n}|^2, \quad (7)$$

where $\hat{n}$ is the unit vector in the polarization direction.

III. INTRODUCING DECOHERENCE INTO TDDFT

A. An open two-level system

Our strategy to incorporate dephasing and decoherence into TDDFT is patterned after open-quantum system approaches developed for the stochastic extension of the time-dependent Schrödinger equation (TDSE) [18,41,42]. Accordingly, the stochastic TDSE contains in addition to the system Hamiltonian H, a stochastically fluctuating system-bath interaction V_k (often referred to as "kicks") which, in general, couples the system to the environment at random times t_i. This stochastic system-bath interaction accounts for both dissipation and fluctuations in line with the dissipation-fluctuation theorem [43]. The time evolution of the state $|\psi(t)\rangle$ is consequently given by an alternating sequence of continuous evolution operators governed by the system Hamiltonian $U(t_{i+1},t_i) = \mathcal{T}\exp(-i\int_{t_i}^{t_{i+1}} H\,dt')$ interrupted by stochastic perturbations described by the evolution operator $U_k^{(j)}$,

$$|\psi^{(j)}(t)\rangle = \prod_i \left[U_k^{(j)}U(t_{i+1},t_i)\right]|\psi(t_0)\rangle. \quad (8)$$

Ensemble averages over M different realizations of the sequence of stochastic interactions $\{|\psi^{(j)}(t)\rangle\}$, referred to as the quantum trajectories, yield the reduced density matrix (RDM),

$$\rho(t) = \frac{1}{M}\sum_{j=1}^{M}|\psi^{(j)}(t)\rangle\langle\psi^{(j)}(t)|, \quad (9)$$

which, for a wide class of stochastic processes, can be shown to obey a Lindblad-type equation of motion [34],

$$\frac{d}{dt}\rho(t) = -i[H,\rho(t)] + T\rho T^\dagger - \frac{1}{2}[T^\dagger T,\rho]_+, \quad (10)$$

with the transition operators $T(T^\dagger)$ induced by V_k representing the system-bath interaction. For effective one-particle quantum trajectories, $\rho(t)$ represents the 1RDM. In the present case of the open-quantum system extension of TDDFT, the starting point is the Kohn-Sham equation of motion [Eq. (1)] rather than the TDSE.

We first illustrate the explicit construction of the relaxation or decoherent dynamics in analogy to that of Eqs. (8) and (10) with the help of a simplified two-level system with the states denoted by $\{|a\rangle, |b\rangle\}$ coupled to an external bath with quantum state $(|s\rangle,\ s = 0,\ldots)$ representing, e.g., a phonon bath. The index s abbreviates the set of all quantum numbers of the bath. In the following $|a\rangle$ and $|b\rangle$ will correspond to valence and conduction band states, respectively. Assuming for simplicity that the phonon bath is initially in its ground state $|s=0\rangle$ (e.g., at zero temperature), the initial nonentangled product state of system and environment may be, in general, a coherent superposition of the valence and conduction-band states,

$$|\psi_0\rangle = \alpha|a,0\rangle + \beta|b,0\rangle, \quad (11)$$

with $|\alpha|^2 + |\beta|^2 = 1$. The initial electronic 1RDM is given by the trace over the phonon degrees of freedom $|s\rangle$,

$$\rho(t_0) = \mathrm{Tr}_s(|\psi_0\rangle\langle\psi_0|) = \begin{pmatrix}|\alpha|^2 & \alpha\beta^*\\ \alpha^*\beta & |\beta|^2\end{pmatrix}. \quad (12)$$

For the initial state [Eq. (11)], $\rho(t_0=0)$, of course, still represents a pure state. The interaction V_k now couples the electronic and phonon degrees of freedom. For sufficiently small interaction time intervals Δt and weak coupling within the Born-Markov limit [44], the amplitudes for state admixtures are given in first-order approximation by time-dependent amplitudes,

$$c_s^{(a)}(\Delta t) = -i\Delta t\langle a,s|V_k|a,0\rangle, \quad (13)$$

$$c_s^{(b)}(\Delta t) = -i\Delta t\langle b,s|V_k|b,0\rangle, \quad (14)$$

resulting in the entangled state,

$$|\psi(\Delta t)\rangle = \alpha\mathcal{N}_a(\Delta t)\left[|a,0\rangle + \sum_{s>0} c_s^{(a)}(\Delta t)|a,s\rangle\right] + \beta\mathcal{N}_b(\Delta t)\left[|b,0\rangle + \sum_{s>0} c_s^{(b)}(\Delta t)|b,s\rangle\right], \quad (15)$$

with renormalization factors,

$$\mathcal{N}_{a,b}(\Delta t) = \left(1 + \sum_{s>0}|c_s^{(a,b)}(\Delta t)|^2\right)^{-1/2}. \quad (16)$$

The total probability for an electron in state $|a\rangle$ (or $|b\rangle$) to induce a transition in the phonon bath during the time interval Δt is $P_j(\Delta t) = 1 - \mathcal{N}_j^2(\Delta t)$ (with $j = a, b$). For suitable choices of the stochastic variable Δt the coupling to the bath [Eq. (15)] allows for the discretization of the system-bath interaction and the introduction of discrete decoherence steps in analogy to Eq. (8). In general, the coupling strength to the environment will depend on the electronic state. In the limit that only the conduction-band state $|b\rangle$ can excite phonons, only $\mathcal{N}_b(\Delta t) < 1$ while $\mathcal{N}_a(\Delta t) = 1$. For the entangled state Eq. (15), after tracing out the phonon degree of freedom the 1RDM after one decoherence step becomes

$$\rho(\Delta t) = \begin{pmatrix}|\alpha|^2 & \alpha\beta^*\mathcal{D}_{ab}(\Delta t)\\ \alpha^*\beta\mathcal{D}^*_{ab}(\Delta t) & |\beta|^2\end{pmatrix}, \quad (17)$$

with

$$\mathcal{D}_{ab}(\Delta t) = \mathcal{N}_a(\Delta t)\mathcal{N}_b(\Delta t)\left(1 + \sum_{s>0} c_s^{(a)}(\Delta t)c_s^{*(b)}(\Delta t)\right) \quad (18)$$

the decoherence factor. Equation (17) represents for all $|\mathcal{D}_{ab}| < 1$ a mixed state and remains a pure state only for $\mathcal{N}_a = \mathcal{N}_b = \mathcal{D}_{ab} = 1$ (i.e., for vanishing phonon coupling). The evolution of ρ [Eq. (17)] during one decohering time step can be formally written as

$$\rho(\Delta t) = \mathscr{R}(\Delta t)\rho(0), \tag{19}$$

in terms of the relaxation superoperator $\mathscr{R}(\Delta t)$ in Liouville space [45,46] with

$$\mathscr{R}_{ij,kl}(\Delta t) = \delta_{ik}\delta_{jl} \times \begin{cases} 1 & (i = j) \\ \mathcal{D}_{ab}(\Delta t) & (i < j) \\ \mathcal{D}^*_{ab}(\Delta t) & (j < i) \end{cases}. \tag{20}$$

In the basis of the time-dependent Kohn-Sham orbitals, $\mathscr{R}(\Delta t)$ will be, in general, explicitly time dependent, i.e., $\mathscr{R}(t, \Delta t)$. For notational simplicity we suppress this dependence in the following. The time evolution of $\rho(t)$ over finite time intervals from $t_0 = 0$ to t can now be formally written in analogy to Eq. (8) by a sequence of alternating steps of smooth evolution governed by the system Hamiltonian and discrete stochastic perturbations due to environmental couplings,

$$\rho(t) = \prod_{i=0}^{m-1} \left\{ \mathscr{R}(\Delta t)\, \mathcal{T} \exp\left[-i \int_{t_i}^{t_{i+1}} dt'\, \mathscr{L}(t') \right] \right\} \rho(t_0 = 0), \tag{21}$$

with $t_m = t$. In Eq. (21), $\mathscr{L}(t)$ denotes the explicitly time-dependent Liouvillian of the unitary evolution, $[H(t), \ldots]$, in between stochastic scatterings requiring the time-ordered ($\mathcal{T}$) exponentiation. Analogously to Eqs. (8) and (10), an ensemble average over stochastic realizations of Eq. (21) should be taken.

B. Decoherence in TDDFT

1. *Generalization to* N *levels*

We now generalize the open two-level system (Sec. III A) to the Kohn-Sham Hamiltonian for the electronic structure in solids. The Kohn-Sham system can be viewed as an ensemble of electronic N-level systems, each member of which corresponds to one discrete $\vec{k}$ (grid) point that is adiabatically shifted by the vector potential. We restrict ourselves in the following to (approximately) quasimomentum conserving scattering processes such as electron-phonon scattering or distant (soft) electron-electron scattering for which the associated quasimomentum transfer is smaller than the k-grid spacing Δk. For each $\vec{k}$ point, the KS system consists of N orbitals $\{|a_1\rangle, \ldots, |a_{N_{\rm vb}}\rangle, |b_1\rangle, \ldots, |b_{N_{\rm cb}}\rangle\}$ with $N_{\rm vb}$ valence band states and $N_{\rm cb}$ conduction band states and $N_{\rm vb} + N_{\rm cb} = N$ being the number of basis functions sufficient to represent all excited states that acquire population during the time propagation. For notational simplicity we drop the index for the $\vec{k}$ point in the following.

The initial state of the system at $t = 0$ is taken to be the ground-state density matrix,

$$\rho(0) = \sum_{n=1}^{N} w_n |\Phi_n(0)\rangle\langle\Phi_n(0)|, \tag{22}$$

with occupation numbers $w_n = 1$ for $1 \leqslant n \leqslant N_{\rm vb}$ and $w_n = 0$ for states in the conduction band. The ground-state KS orbitals ($|\Phi_n^{\rm GS}\rangle = |\Phi_n(0)\rangle$) also coincide with the natural orbitals, a property which is lost after the first decoherence step (see below). At any time during the time evolution we expand the KS orbitals in the Houston basis [Eq. (4)] denoted by $\{|a_i\rangle, |b_i\rangle\}$ representing the field-shifted valence $\{|a_i\rangle\}$ and conduction band $\{|b_i\rangle\}$ states. Generalizing Eq. (11) the states of the combined system of electronic states and environmental degrees of freedom (e.g., phonons) prior to a decohering scattering event read,

$$|\psi_n\rangle = |\Phi_n, 0\rangle = \sum_{i=1}^{N_{\rm vb}} \alpha_{in}|a_i, 0\rangle + \sum_{i=1}^{N_{\rm cb}} \beta_{in}|b_i, 0\rangle, \tag{23}$$

with $\sum_{i=1}^{N_{\rm vb}} |\alpha_{in}|^2 + \sum_{i=1}^{N_{\rm cb}} |\beta_{in}|^2 = 1$. Since the Houston states are capable of adiabatically following the strong-field perturbation and couple dynamically only through "high" frequency components of the field driving transitions among them, they are well suited to act as "pointer states" [32], i.e., the preferred basis with respect to which off-diagonal elements of the density matrix,

$$\rho(t) = \begin{pmatrix} \rho_{1\,1} & \rho_{1\,2} & \cdots & \rho_{1\,N_{\rm vb}} & \rho_{1\,N_{\rm vb}+1} & \cdots & \rho_{1\,N} \\ \rho_{2\,1} & \rho_{2\,2} & \cdots & \rho_{2\,N_{\rm vb}} & \rho_{2\,N_{\rm vb}+1} & \cdots & \rho_{2\,N} \\ \vdots & \vdots & \ddots & \vdots & \vdots & & \vdots \\ \rho_{N_{\rm vb}\,1} & \rho_{N_{\rm vb}\,2} & \cdots & \rho_{N_{\rm vb}\,N_{\rm vb}} & \rho_{N_{\rm vb}\,N_{\rm vb}+1} & \cdots & \rho_{N_{\rm vb}\,N} \\ \rho_{N_{\rm vb}+1\,1} & \rho_{N_{\rm vb}+1\,2} & \cdots & \rho_{N_{\rm vb}+1\,N_{\rm vb}} & \rho_{N_{\rm vb}+1\,N_{\rm vb}+1} & \cdots & \rho_{N_{\rm vb}+1\,N} \\ \vdots & \vdots & & \vdots & \vdots & \ddots & \vdots \\ \rho_{N\,1} & \rho_{N\,2} & \cdots & \rho_{N\,N_{\rm vb}} & \rho_{N\,N_{\rm vb}+1} & \cdots & \rho_{N\,N} \end{pmatrix}, \tag{24}$$

will decohere. The off-diagonal entries depicted in green in Eq. (24) describe valence intraband coherences, red entries corresponding to conduction-band intraband coherences, and blue entries to interband coherences. Accordingly, we construct the relaxation superoperator $\mathscr{R}(t, \Delta t)$ for the density matrix in the Houston basis. The scattering probabilities for a particle in a valence band orbital, $P_{a_i}(\Delta t) = 1 - \mathcal{N}_{a_i}^2(\Delta t)$, and for a particle in a conduction band orbital, $P_{b_i}(\Delta t) = 1 - \mathcal{N}_{b_i}^2(\Delta t)$, will, in general, be different (typically $\mathcal{N}_{a_i}(\Delta t) > \mathcal{N}_{b_i}(\Delta t)$) and orbital ($i$) and $\vec{k}$ dependent. Simple approximations for scattering rates can be derived from, e.g., mean free paths for electron-phonon, electron-defect, or distant electron-electron scattering. Generalizing Eq. (20), the matrix elements of $\mathscr{R}(\Delta t)$ follow from Eq. (23) as

$$\mathscr{R}_{ij,kl}(\Delta t) = \delta_{ik}\delta_{jl} \times \begin{cases} 1 & (i = j) \\ \mathcal{D}_{a_i a_j}(\Delta t) & (i < j \leqslant N_{\mathrm{vb}}) \\ \mathcal{D}^*_{a_i a_j}(\Delta t) & (j < i \leqslant N_{\mathrm{vb}}) \\ \mathcal{D}_{a_i b_j}(\Delta t) & (i \leqslant N_{\mathrm{vb}} < j) \\ \mathcal{D}^*_{a_i b_j}(\Delta t) & (j \leqslant N_{\mathrm{vb}} < i) \\ \mathcal{D}_{b_i b_j}(\Delta t) & (N_{\mathrm{vb}} < i < j \leqslant N) \\ \mathcal{D}^*_{b_i b_j}(\Delta t) & (N_{\mathrm{vb}} < j < i \leqslant N) \end{cases} \tag{25}$$

with

$$\mathcal{D}_{a_i a_j}(\Delta t) = \mathcal{N}_{a_i}(\Delta t)\mathcal{N}_{a_j}(\Delta t)\left(1 + \sum_{s>0} c_s^{(a_i)}(\Delta t) c_s^{*(a_j)}(\Delta t)\right), \tag{26}$$

$$\mathcal{D}_{a_i b_j}(\Delta t) = \mathcal{N}_{a_i}(\Delta t)\mathcal{N}_{b_j}(\Delta t)\left(1 + \sum_{s>0} c_s^{(a_i)}(\Delta t) c_s^{*(b_j)}(\Delta t)\right), \tag{27}$$

$$\mathcal{D}_{b_i b_j}(\Delta t) = \mathcal{N}_{b_i}(\Delta t)\mathcal{N}_{b_j}(\Delta t)\left(1 + \sum_{s>0} c_s^{(b_i)}(\Delta t) c_s^{*(b_j)}(\Delta t)\right). \tag{28}$$

Analogously to Eq. (21), the time evolution of the density operator is now formally given by

$$\rho(t) = \prod_{i=0}^{m-1} \left\{ \mathscr{R}(\Delta t)\, \mathcal{T} \exp\left[-i \int_{t_i}^{t_{i+1}} dt'\, \mathscr{L}_{\mathrm{KS}}(t') \right] \right\} \rho(t_0), \tag{29}$$

with $\mathscr{L}_{\mathrm{KS}}(t')$ the time-dependent Liouvillian acting on the Kohn-Sham system. After each application of the relaxation operator the density matrix is decomposed into a sum of dyadic products of new orbitals $|\Phi'_n(t_i)\rangle$ with new weights w'_n,

$$\rho(t_i) = \sum_{n=1}^{N} w'_n |\Phi'_n(t_i)\rangle\langle\Phi'_n(t_i)|, \tag{30}$$

which are further propagated during the next time step using the KS Hamiltonian. In general, an ensemble average over stochastic realizations of Eq. (29) is required.

2. Numerical implementation

For the implementation of the protocol outlined above [Eqs. (22)–(30)] Houston orbitals acting as "pointer states" are required as input. They should be calculated before each decoherence step by diagonalization of the (GS) KS Hamiltonian shifted in reciprocal space for each quasimomentum associated with the instantaneous vector potential $\vec{k}_0 + \vec{A}(t)$. As recalculating Houston orbitals for each step is extremely time-consuming, in the present implementation we prepare KS orbitals prior to the TDDFT propagation on a very fine $\vec{k}$ grid with spacing $\Delta k = 6 \times 10^{-4}$ a.u. along the polarization direction of the laser pulse. During the propagation, Houston orbitals pertaining to the continuously distributed quasimomentum $\vec{k}_0 + \vec{A}(t)$ [Eq. (23)] are approximated by those KS orbitals at the closest grid point $\vec{k} \approx \vec{k}_0 + \vec{A}(t)$. This approximation significantly speeds up the calculation but introduces a small discretization error. The algorithm employed to correct for this discretization error is described in Appendix A.

We simplify solving Eq. (29) by taking the following steps: First, we solve the real-space real-time Kohn-Sham equations for the $N = N_{\mathrm{vb}} + N_{\mathrm{cb}}$ orbitals $u_n(\vec{r}, t_i) = \langle \vec{r} \,|\Phi_n(t_i)\rangle$ from time t_i to t_{i+1} with the density in $\hat{H}^{\mathrm{KS}}[n(\vec{r}, t)]$ calculated using the weights w_n, $n(\vec{r}, t) = \sum_{n=1}^{N} w_n |u_n(\vec{r}, t)|^2$. After five time steps we apply the decoherence operator $\mathscr{R}(\Delta t)$ at time t_{i+1} to account for decoherence accumulated over the period $\Delta t = t_{i+1} - t_i = 5 \times \Delta t_{\mathrm{TDDFT}} = 0.075$ a.u. We replace in the following the ensemble average over different realizations by one single "representative" time propagation using a fixed Δt. Variation of the precise value of Δt have been found to leave the numerical results unchanged as long as $\Delta t \ll \tau_{\mathrm{dec}}$. Application of the decoherence step after Δt results in a changed density matrix $\rho(t_{i+1})$ and a new set of weights and orbitals, $\sqrt{w_n}|\Phi_n(t_{i+1})\rangle \xrightarrow{\mathscr{R}(\Delta t)} \sqrt{w'_n}|\Phi'_n(t_{i+1})\rangle$.

As discussed above, $\mathcal{N}_{a_i}(\Delta t)$ and $\mathcal{N}_{b_i}(\Delta t)$ will in general depend on the orbital i and momentum $\vec{k}$. For the simple test calculations shown here and for the direct comparison with the results of the BE for the TD-1RDM we use $\mathcal{N}_{a_i}(\Delta t) = 1$ and $\mathcal{N}_{b_i}(\Delta t) = \mathcal{N}(\Delta t)$ independent of i and $\vec{k}$ for all $i \in \{1, \ldots, N_{\mathrm{cb}}\}$, corresponding to an effective decoherence time $\tau_{\mathrm{dec}} \simeq \frac{\Delta t}{1-\mathcal{N}(\Delta t)}$. This implies that the blue and red entries in Eq. (24) are damped per decoherence step by $e^{-\Delta t/\tau_{\mathrm{dec}}}$ and $e^{-2\Delta t/\tau_{\mathrm{dec}}}$, respectively, while green entries remain unchanged. Note that when using microscopic input [Eqs. (26)–(28)] rather than this model input, deviations from a simple exponential decay are to be expected. Using the numerical procedure described in Appendix A inclusion of decoherence increases the CPU time for propagation compared to the TDDFT propagation by about a factor of 4 while maintaining a high level of numerical accuracy. The present implementation of decoherence is conceptually independent of the level of sophistication employed for the underlying TDDFT, in particular of the choice of the exchange-correlation potential V_{XC}. In addition to the A-LDA we have also tested the Tran-Blaha-mBJ approximation for the V_{XC} featuring the correct band gap of diamond [47]. While the enlarged band gap accommodates additional band-gap harmonics, the change in the XC potential leaves the effect of decoherence largely unchanged. For reasons of computational efficiency we have used the A-LDA V_{XC} for the numerical results presented below.

C. Bloch equations in the Houston basis

For a comparison with previously employed methods for incorporating decoherence in driven solid-state electron dynamics, we propagate the one-particle reduced density matrix $\rho^{\vec{k}}_{mn}$ in the Houston basis [Eq. (4)] by solving the Bloch equations for centro-symmetric systems,

$$\partial_t \rho^{\vec{k}}_{mn} = -i\omega^{\vec{k}+\vec{A}(t)}_{mn}\rho^{\vec{k}}_{mn} + i\vec{F}(t)\sum_l \left(\vec{d}^{\vec{k}+\vec{A}(t)}_{ml}\rho^{\vec{k}}_{ln} - \vec{d}^{\vec{k}+\vec{A}(t)}_{ln}\rho^{\vec{k}}_{ml}\right) - (1-\delta_{mn})\frac{\rho^{\vec{k}}_{mn}}{\tau_{mn}}, \tag{31}$$

for a dense set of $\vec{k}$ points initially in the first Brillouin zone and shifted in reciprocal space in time by the quasimomentum associated with the vector potential. The last term in Eq. (31) represents the loss of coherence between bands m and n with decoherence time τ_{mn} corresponding to the "transverse" relaxation time T_2. The "longitudinal" relaxation time is quite long, $T_1 \gg T_2$, and does not affect the evolution of the 1RDM over time scales relevant for this work (a few tens of femtoseconds) and is omitted. For weak to moderate laser intensities where the electronic system is still close to its ground state and a strong nonlinear response is not yet expected to significantly modify the band structure and introduce dynamical correlation effects, the BE approach to the TD-1RDM [Eq. (31)] is expected to closely match the OQS-TDDFT results if the same input from ground-state DFT calculations is used. Accordingly, the transition frequencies $\omega^{\vec{k}}_{mn} = \varepsilon_{m\vec{k}} - \varepsilon_{n\vec{k}}$ and the dipole matrix elements,

$$\vec{d}^{\,\vec{k}}_{mn} = \begin{cases} i\frac{\vec{p}^{\vec{k}}_{mn}}{\omega^{\vec{k}}_{mn}}, & \omega^{\vec{k}}_{mn} \neq 0 \\ 0, & \omega^{\vec{k}}_{mn} = 0 \end{cases}, \tag{32}$$

are extracted from the set of KS orbitals used as the initial state of TDDFT. We emphasize that accurate input from 3D electronic structure calculations, in particular near avoided crossings, for both the band structure and the magnitude and phase of the coupling matrix is essential to reach agreement. Simplified and reduced dimensionality models can achieve qualitative agreement at best.

For the decoherence times we choose in line with our OQS-TDDFT calculation,

$$\tau_{mn} = \begin{cases} \infty, & m,n \notin \mathrm{CB} \\ \tau_{\mathrm{dec}}, & \text{else} \\ \tau_{\mathrm{dec}}/2, & m,n \in \mathrm{CB} \end{cases}. \tag{33}$$

The induced current density corresponding to Eq. (6) is given in terms of the TD-1RDM by

$$\vec{J}(t) \propto \sum_{\vec{k}}\sum_{m,n} \vec{p}^{\vec{k}+\vec{A}(t)}_{mn}\rho^{\vec{k}}_{mn}, \tag{34}$$

and can be separated into intraband ($m = n$) and interband ($m \neq n$) contributions $\vec{J}^{\mathrm{intra}}$ and $\vec{J}^{\mathrm{inter}}$, respectively, allowing for a detailed analysis of inter- and intraband HHG applying Eq. (7) to $\vec{J}^{\mathrm{intra}}$ and $\vec{J}^{\mathrm{inter}}$. This clear separation is, again, consequence of the fact that we formulate the BEs in the Houston basis.

For the BE calculations shown in this work we use a Cartesian $\vec{k}$ grid with step size 0.01 a.u. and 0.07 a.u. parallel and orthogonal to the polarization direction of the laser, respectively. To accurately resolve narrow avoided crossings in the band structure, the transition frequencies and dipole matrix elements are calculated on an extremely fine $\vec{k}$ grid with spacing 0.0003 a.u. taken from the DFT ground state. The time evolution of the BEs composed of four valence and four conduction bands is calculated with a fourth-order Runge-Kutta propagator with a time step of $\Delta t_{\mathrm{RK}} = 0.1$ a.u. It should be noted that by neglecting the self-consistent response of the N-electron system the TD-1RDM approach to the propagation is computationally much faster (by a factor of $\sim 10^3$) than OQS-TDDFT but at the price of a very time-consuming calculation of consistent sets of initial-state coupling-matrix elements and band structures on much finer $\vec{k}$ grids.

IV. COMPARISON BETWEEN OQS-TDDFT AND BLOCH EQUATIONS

In order to test the applicability of the newly developed OQS-TDDFT, we present a detailed quantitative comparison between the induced currents, the resulting HHG calculated with both BE and OQS-TDDFT employing identical input for band-structure and decoherence times, and the response of wide band-gap materials to strong field driving. We choose moderately intense laser pulses in the ir [$\lambda = 800$ nm, 12 cycles total pulse duration $\tau_{\mathrm{ir}} \approx 32$ fs with a $\sin^2$ envelope of the vector potential corresponding to a pulse duration of $\tau \approx 12$ fs of the full width at half maximum (FWHM) of the intensity] and mid-ir ($\lambda = 3200$ nm, eight cycles total pulse duration $\tau_{\mathrm{mir}} \approx 85.4$ fs and $\tau \approx 31$ fs of the FWHM of the intensity] frequency ranges irradiating diamond as a prototypical target material with a band gap of about 5 eV well beyond the one-photon energies of the laser pulses. Additional mesoscopic propagation effects which we have shown to be important for a realistic quantitative comparison with the experiment [12] are intentionally omitted from the present calculation aiming at benchmarking the effect of decoherence on the microscopic dynamics.

We start this section by an analysis of the *linear* response of diamond as determined by time propagation of the "kicked" system allowing for a simple numerical test of our implementation of OQS-TDDFT and for the determination of a lower bound for the decoherence time τ_{dec}.

A. Linear response properties of diamond

The term TDDFT is used for two different settings: on the one hand for the calculation of the linear response (LR) of materials using Kohn-Sham orbitals from a ground-state DFT calculation (LR-TDDFT; for solids see, e.g., [48,49]) and, on the other hand, for the time propagation of Kohn-Sham orbitals as discussed in this paper. Usually, linear-response properties of solids, e.g., the oscillator strengths for excitations from the ground state, are calculated using the former method. Here, we use the real-time propagation method after excitation of the extended system by a δ-shaped electric pulse or, equivalently, a step function in the vector potential, $\vec{A}(t) = \vec{A}_0\theta(t)$. For small step heights, $A_0 \simeq 0.001$ a.u., the system remains well within the regime of linear response and one can

deduce the dielectric function of the material,

$$\varepsilon(\omega) = 1 + i\,\frac{4\pi\sigma(\omega)}{\omega}, \tag{35}$$

with the frequency-dependent conductivity $\sigma(\omega)$ derived from Ohm's law,

$$\sigma(\omega) = -J(\omega)/A_0, \tag{36}$$

and $J(\omega)$ the Fourier transform of the oscillating current $J(t)$. Starting from the ground state, $J(t)$ induced by the constant vector potential A_0 along the polarization direction results exclusively from interband excitations. When accounting for decoherence with energy and momentum independent decoherence time $\tau_{\rm dec} = \text{const}$ exponential damping of the induced current $J(t)$ allows for a direct comparison of results from conventional and OQS-TDDFT. Our simulations using OQS-TDDFT and TDDFT confirm that the induced current accounting for decoherence $J_{\rm dec}(t) \equiv J^{\rm OQS}_{\tau_{\rm dec}}(t) = J^{\rm TDDFT}(t)e^{-t/\tau_{\rm dec}}$ to within numerical accuracy, thus confirming the correct numerical implementation of decoherence in OQS-TDDFT. We compare the simulated linear-response properties of LDA diamond close to the band-gap energy (onset of absorption) by plotting the loss function for different decoherence times $\tau_{\rm dec}$ together with experimental data given by

$$\mathrm{Im}\left[-\frac{1}{\varepsilon(\omega)}\right] = \frac{2n\kappa}{(n^2+\kappa^2)^2}, \tag{37}$$

with

$$\varepsilon(\omega) = (n^2 - \kappa^2) + i2n\kappa, \tag{38}$$

where $n(\omega)$ and $\kappa(\omega)$ are the energy-dependent refractive index and extinction coefficient, respectively. $n(\omega)$ and $\kappa(\omega)$ have been measured for many materials and are readily available from data tables (e.g., [50]).

Due to the small step height A_0 of the vector potential the results of the LR calculations are extremely sensitive to the $\vec{k}$-grid density. We find that the k spacing capable of reaching convergence in simulations of induced electron dynamics in the strong-field regime (see Sec. II and results below) is still insufficient to obtain realistic loss functions in the linear response limit of very weak A_0. We have therefore increased for the linear-response simulation the $\vec{k}$-grid density by setting $\Delta k_\perp = 0.03$ a.u. (instead of $\Delta k_\perp = 0.07$ a.u.).

Figure 1 shows the loss functions calculated by TDDFT ($\tau_{\rm dec} \to \infty$) and OQS-TDDFT for $\tau_{\rm dec} = 10$ fs. The experimental data [50] have been horizontally shifted by 1.45 eV to compensate for the well-known underestimate of the band gap by LDA. The onset of absorption (steepness, step height) is well reproduced by both simulations. Sharp edges in the loss function are smoothed in the presence of decoherence. From the comparison with the experiment near the absorption edge it is obvious that the decoherence time $\tau_{\rm dec}$ should be well above 10 fs. We use $\tau_{\rm dec} = 10$ fs in the remainder of this work as a lower bound taking into account that increasing the excitation density is expected to open additional channels for decoherence thereby possibly slightly decreasing $\tau_{\rm dec}$. Preliminary measurements of the transmission of single pulses as a function of the intensity [51] indicate that an effective decoherence time $\tau_{\rm dec} = 10$ fs corresponding to a scattering

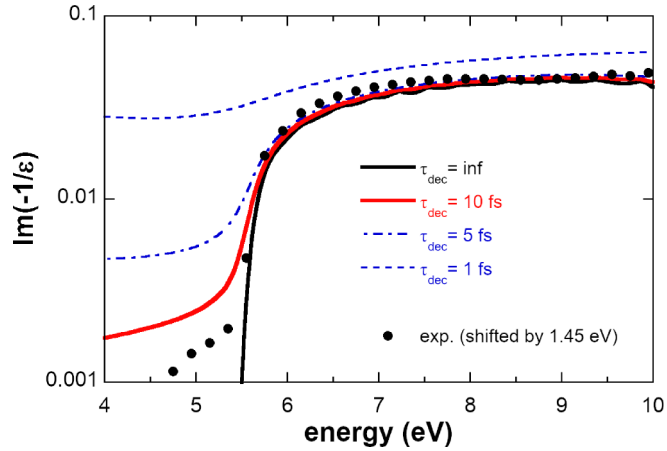

FIG. 1. Simulated (lines) and experimental (symbols) loss functions of diamond. Experimental data have been horizontally shifted by 1.45 eV to correct for the LDA band-gap error. Simulations have been performed using TDDFT (without decoherence, $\tau_{\rm dec} \to \infty$, black lines) and OQS-TDDFT (strong decoherence, $\tau_{\rm dec} = 10$ fs, red line; $\tau_{\rm dec} = 5$ and 1 fs, blue dash-dotted and dashed lines, respectively).

rate of 0.1 fs^{-1} still considerably overestimates the decoherence rate in high quality diamond crystals even for intense pulses with intensities of the order of 10^{13} W/cm^2. Shorter decoherence times (blue lines in Fig. 1) lead to unphysical results highlighted by the complete disappearance of the band gap for $\tau_{\rm dec} \simeq 1$ fs.

One key advantage of the time-propagation method over LR-TDDFT is the possibility to calculate the change of the dielectric properties induced in the material by a time-dependent external potential beyond linear response. We illustrate the potential of this method with the help of the following example (Fig. 2). For a mid-ir laser pulse with $\lambda = 3200$ nm and peak intensity of $I_0 = 5 \times 10^{12}$ with a total duration of eight

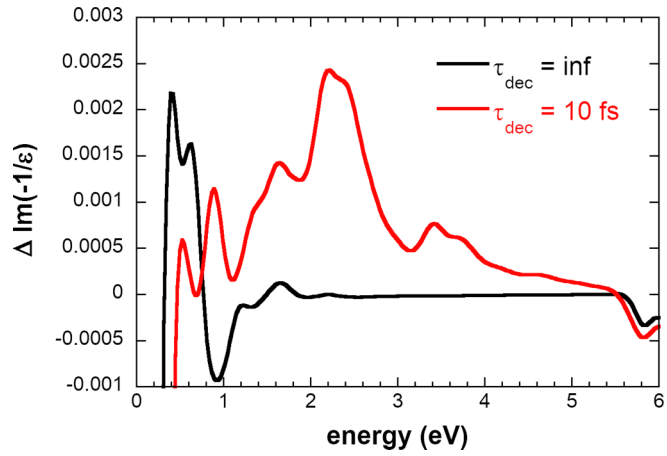

FIG. 2. Change of loss function relative to the ground-state response, $\Delta\,\mathrm{Im}(-1/\varepsilon)$, induced by irradiation of diamond by a 3200-nm laser pulse with $I_0 = 5 \times 10^{12}$ W/cm^2. Due to the small excitation density changes are small on an absolute scale (see Fig. 1). However, large relative differences are found between the coherent ($\tau_{\rm dec} \to \infty$) and decoherent dynamics ($\tau_{\rm dec} = 10$ fs)

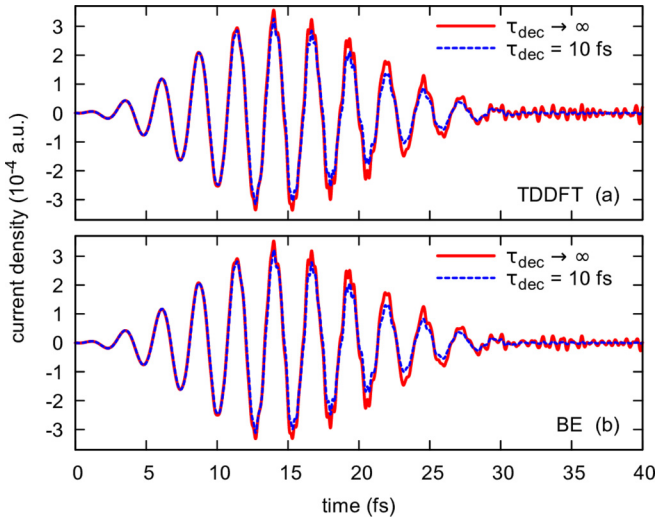

FIG. 3. Current density in diamond induced by an ir laser pulse ($\lambda = 800$ nm, $I_0 = 10^{13}$ W/cm^2, total duration 12 cycles) calculated with (dashed blue lines) and without (red solid lines) decoherence using (a) OQS-TDDFT and (b) Bloch equations (BE).

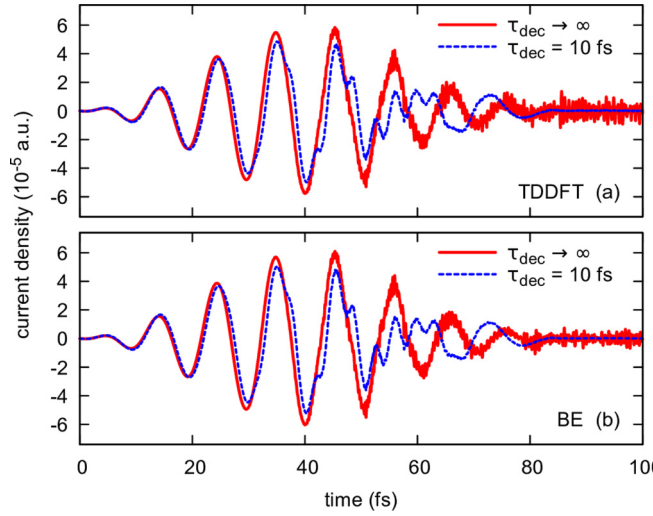

FIG. 4. Same as Fig. 3 but for a mid-ir laser pulse ($\lambda = 3200$ nm, $I_0 = 5 \times 10^{12}$ W/cm^2, total duration eight cycles); (a) TDDFT, (b) BE.

cycles we have first performed the time propagation of the system both in the absence ($\tau_{dec} \to \infty$) and in the presence of strong decoherence ($\tau_{dec} = 10$ fs). At the conclusion of the pulse we set all off-diagonal elements of the density matrix in the Houston basis which for $\vec{A} = 0$ is equivalent to the KS basis to zero thereby neglecting all intraband and interband coherences. This can be viewed as an incoherently excited electronic system with nonvanishing conduction band population. We then probe the linear response of this out-of-equilibrium system by a δ pulse. As expected, an excitation density present in the conduction band after the conclusion of the laser pulse leads to the opening of additional loss channels in the band gap. While the absolute value of the induced change is rather small the simulations show qualitatively different results for $\tau_{dec} \to \infty$ and $\tau_{dec} = 10$ fs indicating the importance of accounting for decoherence in time-dependent systems to determine out-of-equilibrium properties.

B. Total induced currents and high-harmonic generation

The temporal profiles of the current densities predicted by the OQS-TDDFT and the BE (Figs. 3 and 4) agree well with each other on an absolute scale, both in the absence ($\tau_{dec} \to \infty$) and in the presence ($\tau_{dec} = 10$ fs) of decoherence. For this test the decoherence time was chosen to represent a lower bound for the electron-phonon scattering time or, equivalently, the upper bound for the phonon-scattering rate in order to assess the overall influence of decoherence on the induced currents and the observables derived from it. In the absence of decoherence the excellent agreement between TDDFT and BEs indicates that even at moderately strong driving laser fields the electronic structure of the ground state still provides a realistic framework for the ensuing electron dynamics. The persistence of this agreement in the presence of decoherence demonstrates that the present OQS-TDDFT converges in the limit of weak to moderately strong perturbation and for phenomenological decoherence times to the Bloch equations with a transverse relaxation time $T_2 = \tau_{dec}$. The influence of decoherence becomes increasingly important at late propagation times $t > \tau_{dec}$ while the pulse is still on. For the few-cycle pulse with $\lambda = 800$ nm (oscillation period $T \approx 2.7$ fs) the current amplitude is only slightly reduced and the major consequence of decoherence is near-complete damping of post-pulse "ringing", i.e., the field-free current gets efficiently attenuated (Fig. 3). These post-pulse fluctuations originate from the excited-state coherences associated with the off-diagonal elements of the density matrix which persist in the absence of interactions with its surroundings. For mid-ir pulses ($\lambda = 3200$ nm) with a cycle period of $T \approx 10.7$ fs, i.e., of the order of τ_{dec}, the influence of decoherence is considerably more dramatic while the pulse is still on (Fig. 4). The induced current is no longer in phase with the driving pulse and its frequency distribution gets considerably modified. The resulting high-harmonic spectra for the ir pulse (Fig. 5) and the mid-ir pulse (Fig. 6) feature a broad irregularly fluctuating distribution for frequencies well above the band gap extending for the mid-ir pulse to near the ~60th harmonic (Fig. 6). Low-order intraband harmonics are increased in intensity by up to an order of magnitude when including decoherence while high-frequency interband harmonics are decreased by a similar amount. However, a well-defined HHG spectrum with pronounced peaks at odd harmonics, as expected for inversion-symmetric crystals, is missing. This feature has been observed previously and was attributed to the neglect of decoherence [5,6,8,13,14]. Only by assuming extremely short decoherence times of the order of 1 fs (or significantly smaller than the cycle period for ir pulses), the onset of a regular HHG spectrum could be recovered. The physical origin of such fast decoherence processes has remained unexplained. We note that such rapid decoherence, if present, would be a major stumbling block for the realization of ultrafast coherent optoelectronics on the femtosecond scale. It could be recently shown [12] that mesoscopic propagation effects of the light field are key to restoring a well-characterized HHG spectrum without the need for invoking such short decoherence times.

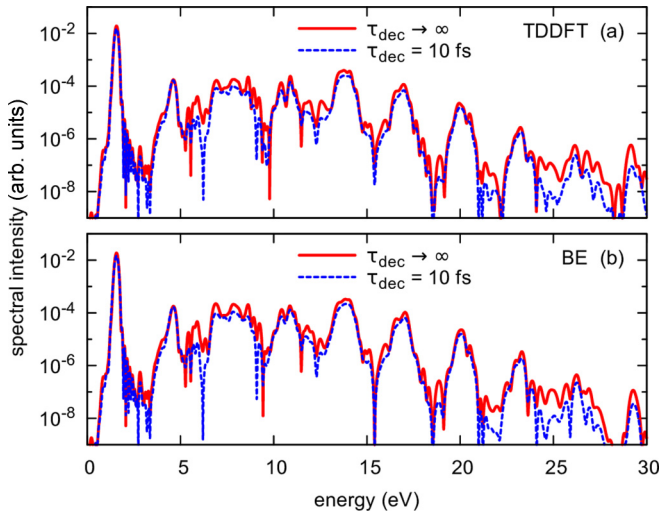

FIG. 5. HHG spectrum derived from the currents shown in Fig. 3 ($\lambda = 800$ nm, $\hbar\omega = 1.55$ eV) calculated with (dashed blue lines) and without (red solid lines) decoherence using (a) OQS-TDDFT and (b) Bloch equations (BE).

The Gabor transform of the signal allowing for a time-frequency analysis of the nonlinear optical response is shown in Fig. 7. The most important effect of decoherence is the strong suppression of the post-pulse high-frequency radiation emitted from the polarization current due to excited-state coherences persistent in the absence of damping. The Gabor transform reveals a pronounced "tilt" of the harmonic peaks above the band gap (upper panels for $\lambda = 800$ nm): Late emission is associated with lower emission energies while early emission corresponds to higher frequencies. This chirp is reminiscent of the contribution from a distribution of "long trajectories" in the semiclassical three-step model of atomic HHG [52,53]. The strong tilt in the present case even leads to an overlap of different harmonic orders when projected onto the frequency axis resulting in the smearing out of well-

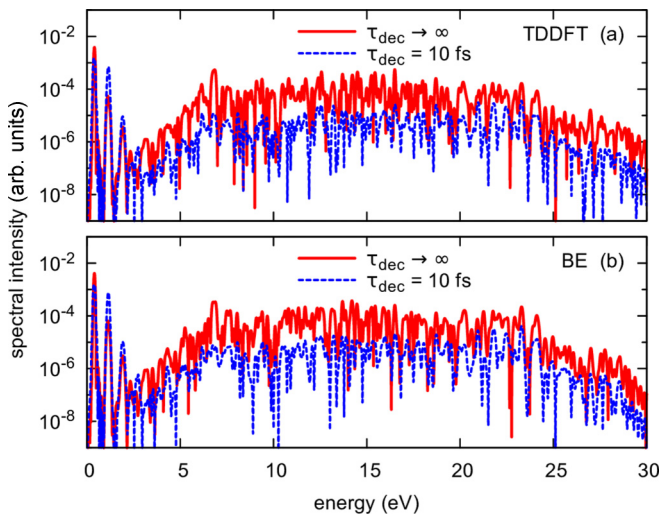

FIG. 6. HHG spectrum derived from the currents shown in Fig. 4 ($\lambda = 3200$ nm, $\hbar\omega = 0.39$ eV) calculated with (dashed blue lines) and without (red solid lines) decoherence using (a) OQS-TDDFT and (b) Bloch equations (BE).

defined peaks at odd harmonics. Only for the low-order band-gap harmonics (<5 in the present case) and for the highest frequencies near the cutoff where only few semiclassical trajectories can contribute a more clearly visible harmonic structure emerges. We note that the present result from OQS-TDDFT closely agrees with corresponding simulations using Bloch equations (not shown).

C. Intra- vs interband currents

The relative importance of intraband and interband current contributions to the HHG spectra has been a topic of lively debate (see, e.g., Ref. [6] vs Ref. [8] and a recent review on solid-state HHG [54]). The driven motion of excited electrons and holes within a given conduction or valence band represents the intraband current. Deviations from a purely parabolic shape of the band give rise to high-frequency components in the current density and, consequently, in the emitted radiation. These contributions strongly depend on the details of the underlying band structure contributing to the current. Moreover, when the vector potential of the pulse is large enough to drive excited carriers across the Brillouin-zone boundary, i.e., $A(t) > \overline{\Gamma X}$, their direction of motion changes resulting in Bloch oscillations contributing to intraband HHG. On the other hand, the coherent excitation of electrons and holes allowing for the coupling between the bands and inducing a rapidly oscillating polarization current gives rise to the interband contribution to HHG. The presence of decoherence can have important implications for the interplay between intraband and interband currents. Figure 8 displays an example for mid-ir driving. The total current drastically changes and gets reduced at late times $t > t_{dec}$. This results from the significant change of the relative weight of the intraband and interband currents which are phase shifted relative to each other by π. In the presence of decoherence [Fig. 8(c)] interband and intraband contributions become comparable for late times while the interband contribution dominates when decoherence is neglected [Fig. 8(b)]. While the maximum vector potential is too small to induce conventional Bloch oscillations, we observe a novel scenario of Bloch oscillations, i.e., reversal of the group velocity, in diamond already for $A(t) \gtrsim \frac{1}{2}\overline{\Gamma X}$ where we find an avoided crossing in the band structure (see Appendix B). Driving an intraband current across this region well inside the Brillouin zone results in a reversal of the carrier velocity in close analogy to that near the Brillouin-zone boundary. The time windows within which the quasimomentum associated with the vector potential exceeds the quasimomentum where the avoided crossing is located is marked in Fig. 8. Within these windows these intra-Brillouin zone Bloch oscillations [dips in the intraband currents in Figs. 8(b) and 8(c)] enhance the intraband current. This demonstrates the importance of using realistic band structures in simulations of HHG in solids instead of simple tight-binding models of the band structure.

The low-energy part of the resulting HHG spectrum (Fig. 9) gives further insight into the interplay between intra- and interband HHG. While the low-order band-gap harmonics (in the present case up to $n = 5$) are dominated by the intraband current, the high harmonics well above the band gap are completely dominated by interband contributions. The

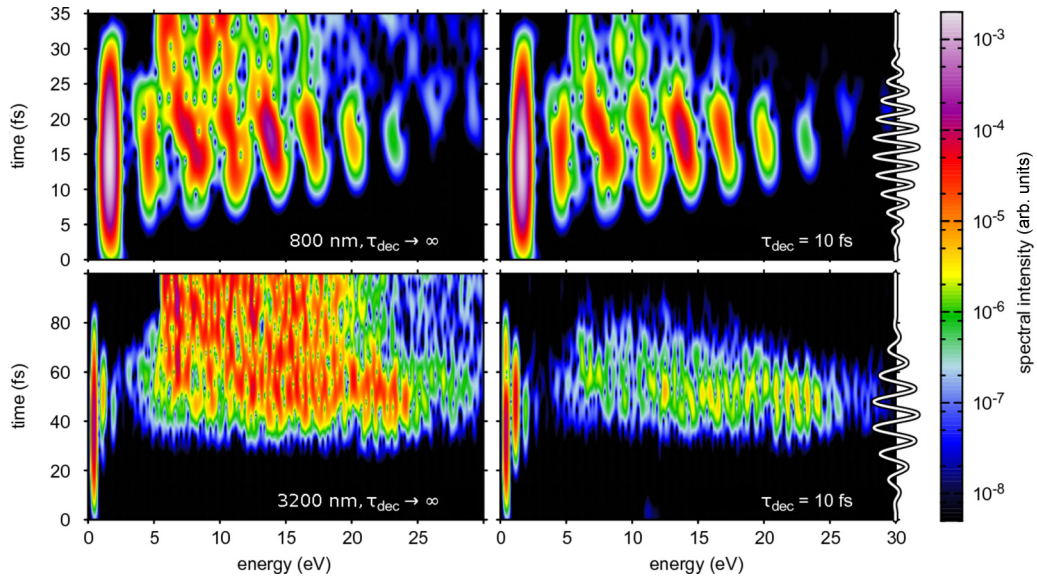

FIG. 7. Time-frequency analysis (Gabor transform) on a logarithmic color scale of the radiation emitted from diamond for an ir pulse (upper row) and a mid-ir pulse (lower row). Left column panels without decoherence; right column with strong decoherence ($\tau_{\rm dec} = 10$ fs). Laser parameters as in Figs. 3 and 4. Width of Gabor wave packet $\sigma = 2$ fs (upper row) and $\sigma = 5$ fs (lower row). Results from the Bloch equations (not shown) closely agree.

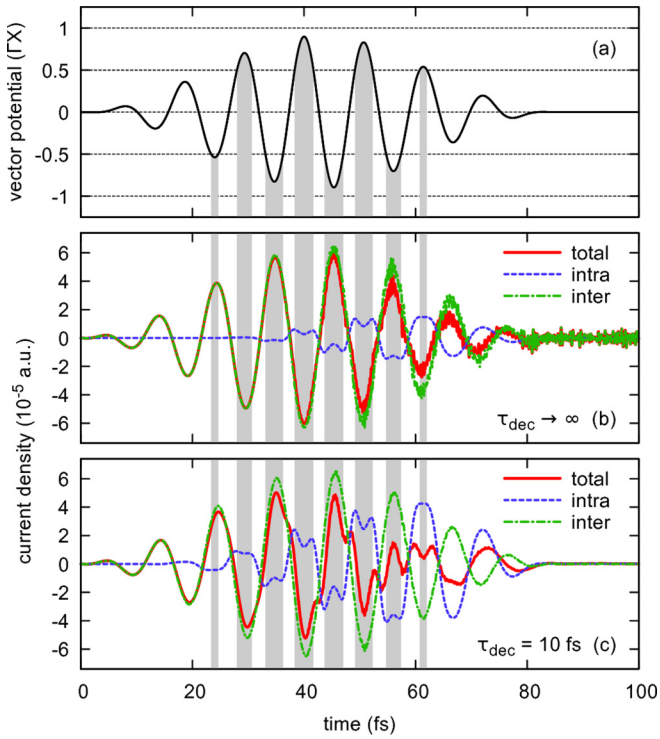

FIG. 8. Separation of intra- and interband currents induced by a mid-ir laser pulse with $\lambda = 3200$ nm, $I_0 = 5 \times 10^{12}$ W/cm^2, and total duration of eight cycles. The time intervals within which the vector potential of the pulse (a) exceeds half the distance to the Brillouin-zone boundary and reaches the avoided crossing, i.e., $|A(t)| > \overline{\Gamma X}/2$, are shaded in gray. The total currents (red solid lines) are decomposed into intraband (blue dashed lines) and interband (green dash-dotted lines) contributions for (b) fully coherent ($\tau_{\rm dec} \to \infty$) and (c) decoherent ($\tau_{\rm dec} = 10$ fs) dynamics. Total currents calculated using TDDFT and BE are (almost) identical; extraction of interband and intraband currents was done from our BE simulation.

relative weight between intraband and interband emission at high frequencies is only marginally affected by the presence of decoherence while we find noticeable changes for the band-gap harmonics.

D. Response to strong-field driving

The present OQS-TDDFT allows one to treat the strongly nonlinear response to strong-field driving accounting for decoherence when the excitation density is sufficiently high and, consequently, the ground-state electronic structure can no longer fully account for the response. During strong-field laser irradiation a significant fraction of the electrons are transiently excited to the conduction band. Most of these electrons are excited close to the peaks of the oscillating electric field of the laser pulse. This can be recorded in terms of an oscillating energy exchange between the radiation field

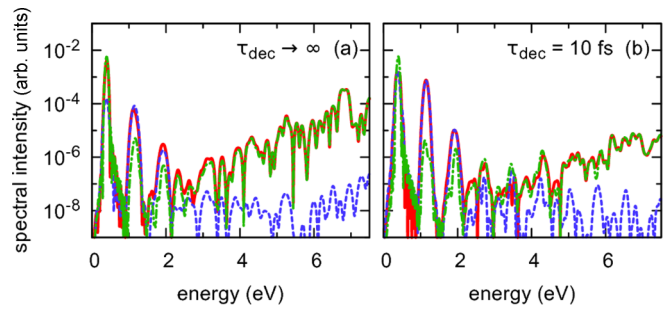

FIG. 9. Decomposition of the total spectrum of the segment of low-order harmonics of Fig. 6 (red solid lines) induced by a mid-ir laser pulse with $\lambda = 3200$ nm, $I_0 = 5 \times 10^{12}$ W/cm^2, and total duration of eight cycles into intraband (blue dashed lines) and interband (green dash-dotted lines) contributions for (a) coherent ($\tau_{\rm dec} \to \infty$) and (b) decoherent dynamics ($\tau_{\rm dec} = 10$ fs).

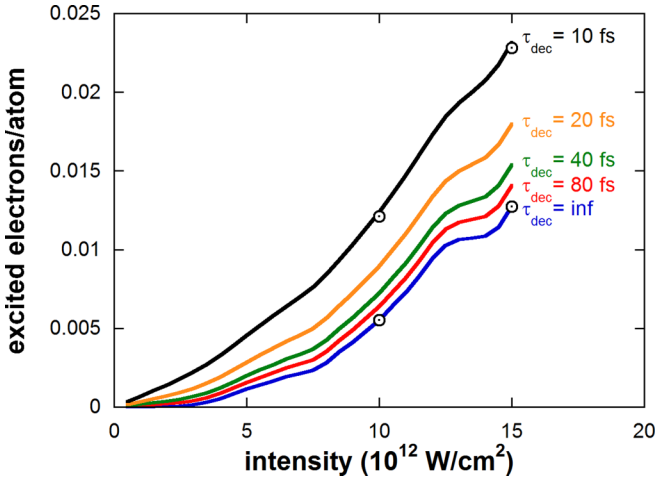

FIG. 10. Carrier excitation density as a function of intensity following a 12-cycle ir pulse with $\lambda = 800$ nm for different decoherence rates calculated using BE. For decoherence times $\tau_{dec} \to \infty$ and $\tau_{dec} = 10$ fs excitation densities have also been calculated using OQS-TDDFT (open circles). Deviations between OQS-TDDFT and BE (solid line) are only about 2% even for short decoherence times and high intensities $I \gtrsim 10^{13}$ W/cm^2.

and the electronic system. Incorporation of dephasing strongly suppresses the coherent deexcitation processes by destroying the well-defined phase relation between particle and hole wave packets to be recombined. As an important consequence the persistent excited carrier density after conclusion of the laser pulse is strongly enhanced. In turn, the optical properties such as the linear-response dielectric function $\varepsilon_{ex}(\omega)$ as well as the nonlinear response of the excited (ex) electronic system are significantly altered compared to the corresponding ground-state response. The resulting excitation density is a function of both the laser intensity and the decoherence rate (Fig. 10). This nonlinear response can be experimentally probed in a pump-probe setting. The excitation density and, in particular, the frequency-dependent transmittivity could be mapped out by a probe pulse arriving subsequently to the strong pump pulse (c.f. Sec. IV A). We find an approximately linear dependence of the excited carriers on the decoherence rates (Fig. 10). Even at intensities close to the destruction limit for diamond (at a vacuum intensity of about $I_0 \sim 2 \times 10^{13}$ W/cm^2) the BE model (solid lines) still closely agrees with the OQS-TDDFT (symbols).

V. CONCLUDING REMARKS

In this work we have presented an open quantum system extension of TDDFT paving the way toward realistic simulations of excited solid-state systems including decohering processes. The basic idea underlying the present approach is to expand the time-dependent Kohn-Sham orbitals into a basis of pointer states of decoherence for which the relaxation operator can be easily constructed. Repeated application of the relaxation (super)operator to the reduced density matrix as the system evolves in time according to the Kohn-Sham equations allows one to consistently account for decoherence effects within TDDFT. We have validated our approach by an in-depth comparison with the solutions of the Bloch equations for the reduced density matrix within which decoherence can be straightforwardly included via a finite dephasing or transverse relaxation time T_2. We have first verified that for the prototypical problem of electron dynamics in diamond driven by moderately strong ultrashort ir and mid-ir laser pulses the induced current and the resulting high-harmonic radiation TDDFT and the BE solutions agree with each other to within the numerical accuracy in the limit of fully coherent dynamics, i.e., in the absence of decoherence. Key to this agreement is that *ab initio* input from the same ground-state DFT calculation that also provides the initial state of the TDDFT simulation is used in the BE calculation. Intra-Brillouin zone Bloch oscillation contributions to intraband harmonics, here identified for the first time, require the accurate representation of the band structure. For moderately strong fields and large band gaps the excitation density remains sufficiently small such that the ground-state electronic structure still governs the nonlinear response to the field. The near-perfect agreement between the TDDFT and BE approaches is found to persist in the presence of decoherence, i.e., for finite T_2, clearly indicating that the present OQS extension of TDDFT allows for the consistent inclusion of dephasing while preserving fundamental properties of TDDFT, in particular conserving particle number density.

In our numerical test cases we have used a constant decoherence time for all excited states of the system to allow for a quantitative comparison between results of OQS-TDDFT with solutions of the Bloch equations. Extensions to state and $\vec{k}$-dependent decoherence times as derived from inelastic mean free paths for decohering processes can be easily implemented. For ultrashort laser pulses with durations comparable to or even shorter than the decoherence times, realistic simulations of the nonlinear electronic response in solids requires the inclusion of decoherence effects. This is also true for long wavelengths and oscillation periods comparable to or longer than the decoherence time. While for large band-gap materials excitation densities after conclusion of the pulse remain small up to laser intensities near the destruction limit of the material allowing for the use of the numerically simpler Bloch equations based on ground-state properties, large excitation densities as expected in metals, and small-band gap semiconductors will require a treatment self-consistently accounting for time-dependent changes induced in the electronic system. The only available method to date capable of performing this task is time-dependent density functional theory. The method presented here allows one to consistently include dephasing processes in solids by interaction with the environment such as, e.g., electron-phonon or electron-defect scattering within TDDFT.

ACKNOWLEDGMENTS

We are grateful to Iva Březinová for helpful discussions. This work was supported by the FWF Austria (SFB-041 ViCoM, SFB-049 NextLite, and doctoral college W1243), and the IMPRS-APS. It was also supported by JSPS KAKENHI Grants No. 16K05495, No. 15H03674, and No. 26-1511, and by CREST, JST, under Grant No. JPMJCR16N5. Calculations were performed using the Vienna Scientific Cluster (VSC)

and the supercomputer at Nagoya University through HPCI (hp160116).

APPENDIX A: ERROR CORRECTION IN THE NUMERICAL IMPLEMENTATION

In our implementation of the decomposition (23) the Houston orbitals at $\vec{k}_0 + \vec{A}(t)$ are approximated by GS orbitals at the closest grid point $\vec{k} \approx \vec{k}_0 + \vec{A}(t)$. Due to the slight mismatch between states at $\vec{k}_0 + \vec{A}(t)$ and $\vec{k}$ a small fraction of the wave function is artificially mapped onto energetically high lying conduction band states. To prevent the incorrect assignment and propagation of these components, we treat them separately from the decoherence step. While the dominant fraction of the wave function is represented within the truncated Houston basis, we store the remaining density incorrectly assigned to higher conduction bands in (non-normalized) auxiliary functions $|h_n\rangle = |h_n, 0\rangle$ with $\langle h_n|h_n\rangle \ll 1$. Accordingly, we expand the KS orbitals [see Eqs. (22) and (23)],

$$\begin{aligned}\sqrt{w_n}|\psi_n\rangle &= \sqrt{\bar{w}_n}|\Phi_n, 0\rangle + |h_n\rangle \\ &= \sum_{i=1}^{N_{\rm vb}} \alpha_{in}|a_i, 0\rangle + \sum_{i=1}^{N_{\rm cb}} \beta_{in}|b_i, 0\rangle + |h_n\rangle, \end{aligned} \tag{A1}$$

prior to the decoherence step. The auxiliary functions $|h_n\rangle$ account for the discretization error and store that part of the wave function not properly represented in the discretized Houston basis. After the decoherence step, we add each $|h_n\rangle$ to the correct modified KS orbitals $|\widetilde{\Phi}_m\rangle$ following the decoherence step. Only close to avoided crossings in the band structure the indices m and n may differ, in most cases $m = n$, as expected.

We adopt the following diagonalization scheme to assure $|\widetilde{\Phi}_m\rangle$ is as close to $|\Phi_n\rangle$ as possible, i.e., to find the correct mapping $m \to n$: Starting from the density matrix after the decoherence step [Eq. (30)] we choose the first state $m = 1$ to include all density-matrix elements which overlap with the energetically lowest Houston state $|a_1\rangle$,

$$\sqrt{\widetilde{w}_1}|\widetilde{\Phi}_1\rangle = \frac{e^{i\varphi_1}}{\sqrt{\rho_{11}}} \begin{pmatrix} \rho_{11} \\ \rho_{21} \\ \vdots \\ \rho_{N1} \end{pmatrix}, \tag{A2}$$

leaving us with the residual density matrix,

$$\begin{aligned}\rho_{\rm R_1} &= \rho - \widetilde{w}_1|\widetilde{\Phi}_1\rangle\langle\widetilde{\Phi}_1| \\ &= \begin{pmatrix} 0 & 0 & \cdots & 0 \\ 0 & \rho_{22} - \frac{\rho_{21}\rho_{12}}{\rho_{11}} & \cdots & \rho_{2N} - \frac{\rho_{21}\rho_{1N}}{\rho_{11}} \\ \vdots & \vdots & \ddots & \vdots \\ 0 & \rho_{N2} - \frac{\rho_{N1}\rho_{12}}{\rho_{11}} & \cdots & \rho_{NN} - \frac{\rho_{N1}\rho_{1N}}{\rho_{11}} \end{pmatrix}, \end{aligned} \tag{A3}$$

where no contributions of $|a_1\rangle$ are left. We then search for the wave function $|\Phi_n\rangle$ before the decoherence step with maximum overlap with $\sqrt{\widetilde{w}_1}|\widetilde{\Phi}_1\rangle$,

$$\max |\sqrt{\bar{w}_n\widetilde{w}_1}\langle\Phi_n|\widetilde{\Phi}_1\rangle|, \tag{A4}$$

to find the correct index n associated with $m = 1$. The phase φ_1 [Eq. (A2)] is chosen such that the relative phase between $|\Phi_n\rangle$ and $|h_n\rangle$ is preserved, i.e., $\langle\Phi_n|\widetilde{\Phi}_1\rangle \in \mathbb{R}^+$, before adding the auxiliary function to the $\sqrt{\widetilde{w}_1}|\widetilde{\Phi}_1\rangle$,

$$\sqrt{w_1'}|\Phi_1'\rangle = \sqrt{\widetilde{w}_1}|\widetilde{\Phi}_1\rangle + |h_n\rangle. \tag{A5}$$

Before calculating the next state $\sqrt{w_2'}|\Phi_2'\rangle$, $|h_n\rangle$ is removed from the set of auxiliary functions.

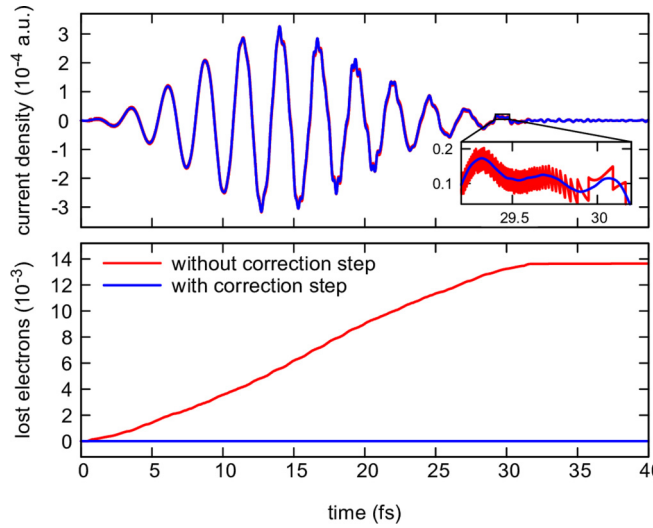

FIG. 11. Current density in diamond induced by a nir laser pulse ($\lambda = 800$ nm, $I_0 = 10^{13}$ W/cm^2, 12 cycles) for $\tau_{\rm dec} = 10$ fs with (blue) and without (red) corrections to the wave function (upper panel). Failure to properly account for discretization errors leads to a maximum accumulated loss of norm of the KS orbitals of $\lesssim$0.1% of the 16 active electrons in the system (lower panel).

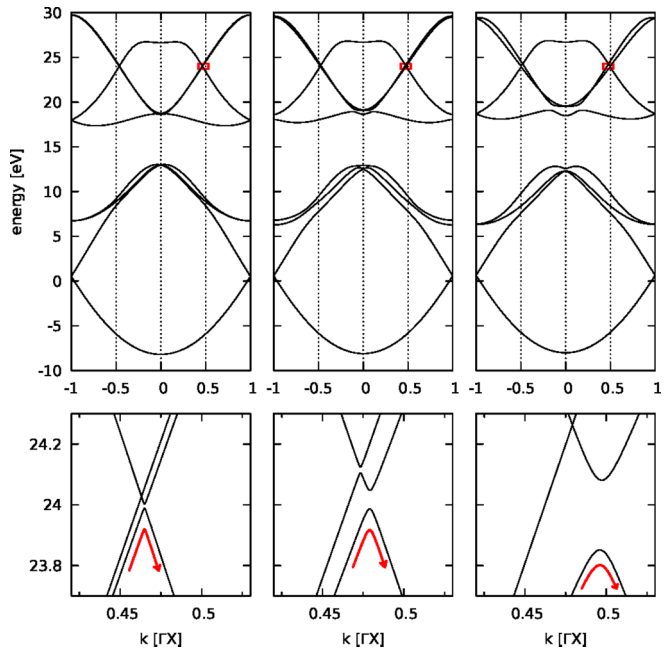

FIG. 12. Band structure of diamond along three lines parallel and close to $\Gamma - X$ and increasing distance to $\Gamma - X$ (from left to right $\Delta k_\perp \approx 0.05, 0.08, 0.15$ a.u.). Bottom panels are magnifications of the band structure in the surrounding of the avoided crossing marked red in upper panels.

This procedure is repeated analogously for all residual matrices ρ_{R_j} resulting in N orbitals $\sqrt{\widetilde{w}_m}|\widetilde{\Phi}_m\rangle$ and new $\sqrt{w'_m}|\Phi'_m\rangle$ which serve as new KS orbitals that are further propagated in time [Eq. (30)] until the next decoherence step occurs. Using the method outlined above, we find perfect agreement in any observables comparing results from our OQS-TDDFT for very long decoherence times $\tau_{\mathrm{dec}} \to \infty$ and from the conventional TDDFT propagation. Applying the correction step, the number of electrons is conserved and no unphysical kinks in the current density are observed (blue lines in Fig. 11). Omitting this correction step, i.e., truncating the basis ($N_{\mathrm{cb}} = 16$) without using the auxiliary functions, leads to an accumulated loss of $\lesssim 0.1\%$ of the active electrons in the system [Fig. 11(b)] corresponding to $\langle h_n|h_n\rangle \lesssim 10^{-7}$ for all times and orbitals. Furthermore, it induces small saw-tooth oscillations in the current density [red line in Fig. 11(a)]. Jumps of the current density indicate transitions between neighboring $\vec{k}$ points on our grid of precalculated approximate Houston states.

APPENDIX B: BAND STRUCTURE OF DIAMOND

As mentioned in Sec. IV C we find reversal of the group velocity of excited electrons for vector potentials much too small to drive occupation from the Γ point to the Brillouin-zone boundary (X). There, further increase of the field strength would induce a jump from $\vec{k} \to -\vec{k}$ in addition to the (possible) sign change of the group velocity $d\varepsilon(k)/dk$ (Bloch oscillation). For diamond we observe sign reversals of the group velocity (intraband current) already at approximately half the field strength necessary to induce Bloch oscillations. Analysis of the band structure of diamond reveals narrow avoided crossings at about half the distance between Γ and X (Fig. 12) with small coupling strengths between neighboring bands for laser polarization parallel to the Γ − X direction. Carrier density reaching the avoided crossing will therefore change the sign of its group velocity with large probability and induce the oscillations observed in the intraband current [Fig. 8(c)].

[1] P. Hohenberg and W. Kohn, Phys. Rev. **136**, B864 (1964).
[2] E. Runge and E. K. U. Gross, Phys. Rev. Lett. **52**, 997 (1984).
[3] K. Yabana, T. Sugiyama, Y. Shinohara, T. Otobe, and G. F. Bertsch, Phys. Rev. B **85**, 045134 (2012).
[4] S. Ghimire, A. D. DiChiara, E. Sistrunk, P. Agostini, L. F. DiMauro, and D. A. Reis, Nat. Phys. **7**, 138 (2011).
[5] O. Schubert, M. Hohenleutner, F. Langer, B. Urbanek, C. Lange, U. Huttner, D. Golde, T. Meier, M. Kira, S. W. Koch, and R. Huber, Nat. Photonics **8**, 119 (2014).
[6] T. T. Luu, M. Garg, S. Y. Kruchinin, A. Moulet, M. T. Hassan, and E. Goulielmakis, Nature (London) **521**, 498 (2015).
[7] G. Vampa, T. J. Hammond, N. Thiré, B. E. Schmidt, F. Légaré, C. R. McDonald, T. Brabec, D. D. Klug, and P. B. Corkum, Phys. Rev. Lett. **115**, 193603 (2015).
[8] G. Vampa, C. R. McDonald, G. Orlando, D. D. Klug, P. B. Corkum, and T. Brabec, Phys. Rev. Lett. **113**, 073901 (2014).
[9] M. Wu, S. Ghimire, D. A. Reis, K. J. Schafer, and M. B. Gaarde, Phys. Rev. A **91**, 043839 (2015).
[10] T. Otobe, Phys. Rev. B **94**, 235152 (2016).
[11] N. Tancogne-Dejean, O. D. Mücke, F. X. Kärtner, and A. Rubio, Phys. Rev. Lett. **118**, 087403 (2017).
[12] I. Floss, C. Lemell, G. Wachter, V. Smejkal, S. A. Sato, X.-M. Tong, K. Yabana, and J. Burgdörfer, Phys. Rev. A **97**, 011401(R) (2018).
[13] F. Langer, M. Hohenleutner, U. Huttner, S. W. Koch, M. Kira, and R. Huber, Nat. Photonics **11**, 227 (2017).
[14] S. Jiang, H. Wei, J. Chen, C. Yu, R. Lu, and C. D. Lin, Phys. Rev. A **96**, 053850 (2017).
[15] K. Burke, R. Car, and R. Gebauer, Phys. Rev. Lett. **94**, 146803 (2005).
[16] M. Di Ventra and R. D'Agosta, Phys. Rev. Lett. **98**, 226403 (2007).
[17] R. D'Agosta and M. Di Ventra, Phys. Rev. B **78**, 165105 (2008).
[18] R. Biele and R. D'Agosta, J. Phys.: Condens. Matter **24**, 273201 (2012).
[19] L. E. Reichl, *A Modern Course in Statistical Physics*, 2nd ed. (Wiley, New York, 1998).
[20] G. Vignale and W. Kohn, Phys. Rev. Lett. **77**, 2037 (1996).
[21] J. F. Dobson, M. J. Bünner, and E. K. U. Gross, Phys. Rev. Lett. **79**, 1905 (1997).
[22] Y. Kurzweil and R. Baer, J. Chem. Phys. **121**, 8731 (2004).
[23] I. V. Tokatly, Phys. Rev. B **71**, 165105 (2005).
[24] D. Lacroix and S. Ayik, Eur. Phys. J. A **50**, 95 (2014).
[25] K. Mølmer and Y. Castin, Quant. Semiclass. Opt.: J. Euro. Opt. Soc. Part B **8**, 49 (1996).
[26] P. M. Dinh, L. Lacombe, P.-G. Reinhard, É. Suraud, and M. Vincendon, Eur. Phys. J. B **91**, 246 (2018).
[27] L. Lacombe, P.-G. Reinhard, P. M. Dinh, and É. Suraud, J. Phys. B **49**, 245101 (2016).
[28] J. Yuen-Zhou, C. Rodríguez-Rosario, and A. Aspuru-Guzik, Phys. Chem. Chem. Phys. **11**, 4509 (2009).
[29] A. Abedi, N. T. Maitra, and E. K. U. Gross, Phys. Rev. Lett. **105**, 123002 (2010).
[30] J. Yuen-Zhou, D. G. Tempel, C. A. Rodríguez-Rosario, and A. Aspuru-Guzik, Phys. Rev. Lett. **104**, 043001 (2010).
[31] D. G. Tempel and A. Aspuru-Guzik, Chem. Phys. **391**, 130 (2011).
[32] W. H. Zurek, Phys. Rev. D **24**, 1516 (1981).
[33] A. G. Redfield, IBM J. Res. Dev. **1**, 19 (1957).
[34] G. Lindblad, Commun. Math. Phys. **48**, 119 (1976).
[35] J. P. Perdew and A. Zunger, Phys. Rev. B **23**, 5048 (1981).
[36] W. V. Houston, Phys. Rev. **57**, 184 (1940).
[37] J. B. Krieger and G. J. Iafrate, Phys. Rev. B **33**, 5494 (1986).
[38] D. M. Wolkow, Z. Phys. **94**, 250 (1935).
[39] N. Troullier and J. L. Martins, Phys. Rev. B **43**, 1993 (1991).
[40] J. D. Jackson, *Classical Electrodynamics* (John Wiley & Sons, New York, 1999).
[41] C. Gardiner and P. Zoller, *Quantum Noise* (Springer-Verlag, Berlin/Heidelberg, 2004).
[42] M. Seliger, C. O. Reinhold, T. Minami, and J. Burgdörfer, Phys. Rev. A **71**, 062901 (2005).
[43] H. B. Callen and T. A. Welton, Phys. Rev. **83**, 34 (1951).
[44] H. Breuer and F. Petruccione, *The Theory of Open Quantum Systems* (Oxford University Press, Oxford, 2002).

[45] H. Gabriel, Phys. Rev. **181**, 506 (1969).
[46] K. Blum, *Density Matrix Theory and Applications* (Springer-Verlag, Berlin/Heidelberg, 2012).
[47] F. Tran and P. Blaha, Phys. Rev. Lett. **102**, 226401 (2009).
[48] G. D. Mahan and K. R. Subbaswamy, *Local Density Theory of Polarizability* (Plenum Press, New York and London, 1990).
[49] A. Liebsch, *Electronic Excitations at Metal Surfaces* (Plenum Press, New York and London, 1997).
[50] E. D. Palik, editor, *Handbook of Optical Constants of Solids* (Academic Press, Cambridge, 1997).
[51] D. Zimin, M. Schultze, and N. Karpowicz (private communication, 2018).
[52] P. B. Corkum, Phys. Rev. Lett. **71**, 1994 (1993).
[53] M. Lewenstein, P. Balcou, M. Y. Ivanov, A. L'Huillier, and P. B. Corkum, Phys. Rev. A **49**, 2117 (1994).
[54] S. Ghimire and D. A. Reis, Nature Physics **15**, 10 (2019).